Original article

Boosting ferroptosis and microtubule inhibition for antitumor therapy via a carrier-free supermolecule nanoreactor

Min Mu [a, 1], Xiaoyan Liang [a, 1], Na Zhao [b], Di Chuan [a], Bo Chen [a], Shasha Zhao [a], Guoqing Wang [c], Rangrang Fan [c], Bingwen Zou [d], Bo Han [b], Gang Guo [a, *]

[a] *State Key Laboratory of Biotherapy and Cancer Center, West China Hospital, Sichuan University, Chengdu, 610041, China*
[b] *Key Laboratory of Xinjiang Phytomedicine Resource and Utilization, Ministry of Education, School of Pharmacy, Shihezi University, Shihezi, Xinjiang, 832002, China*
[c] *Department of Neurosurgery, West China Hospital, Sichuan University, Chengdu, 610041, China*
[d] *Department of Radiation Oncology, Cancer Center, West China Hospital, Sichuan University, Chengdu, 610041, China*

ARTICLE INFO

ABSTRACT

Traditional microtubule inhibitors fail to significantly enhance the effect of colorectal cancer; hence, new and efficient strategies are necessary. In this study, a supramolecular nanoreactor (DOC@TA-Fe^{3+}) based on tannic acid (TA), iron ion (Fe^{3+}), and docetaxel (DOC) with microtubule inhibition, reactive oxygen species (ROS) generation, and glutathione peroxidase 4 (GPX4) inhibition, is prepared for ferroptosis/apoptosis treatment. After internalization by CT26 cells, the DOC@TA-Fe^{3+} nanoreactor escapes from the lysosomes to release payloads. The subsequent Fe^{3+}/Fe^{2+} conversion mediated by TA reducibility can trigger the Fenton reaction to enhance the ROS concentration. Additionally, Fe^{3+} can consume glutathione to repress the activity of GPX4 to induce ferroptosis. Meanwhile, the released DOC controls microtubule dynamics to activate the apoptosis pathway. The superior in vivo antitumor efficacy of DOC@TA-Fe^{3+} nanoreactor in terms of tumor growth inhibition and improved survival is verified in CT26 tumor-bearing mouse model. Therefore, the nanoreactor can act as an effective apoptosis and ferroptosis inducer for application in colorectal cancer therapy.

1. Introduction

Microtubules are found in almost all eukaryotic cells. As one of the main components of the cytoskeleton, microtubules play an important role in cell morphology maintenance, intracellular material transport, cell division and differentiation, and other physiological processes [1–3]. Tubulin has become an important target for the research and development of new anticancer drugs [4]. Tubulin inhibitors acting on the microtubule system have also become an effective class of antitumor drugs [5,6]. Docetaxel (DOC), a tubulin inhibitor, has a high affinity for microtubules or tubulin to regulate microtubule dynamics, especially during the vulnerable mitotic stage in the cell cycle [5,7,8]. Although DOC has a significant effect on cancer treatment, single-drug therapies fail to satisfy the clinical application in long-term treatment. Many efforts have been recently devoted to combining microtubule inhibitors with other strategies, and promising results have been obtained for cancer therapy [7,9].

Ferroptosis, a new iron-dependent regulated form of cell death, is distinct from apoptosis, autophagy, and necrosis [10,11]. A series of studies were conducted to induce ferroptosis by delivering exogenous iron to the tumor site [12–17]. The Fenton reaction activity of iron ion (Fe^{3+}) is several magnitudes lower than that of ferrous ion (Fe^{2+}), and insufficient intracellular iron levels severely hinder the effect of ferroptosis [18,19]. Apart from iron metabolism, the intervention of glutathione peroxidase 4 (GPX4) can trigger ferroptosis [20]. GPX4 inactivation by depleting glutathione (GSH) with Fe^{3+} to convert to oxidized glutathione disulfide ultimately results in ferroptotic cell death [21,22]. In this regard, delivering Fe^{3+} to deplete GSH and convert Fe^{2+} may be a promising tactic for ferroptosis therapy. We speculated that combining ferroptosis and microtubules may be a great idea to induce tumor cell death. Although certain amounts of Fe are necessary to trigger ferroptosis, abnormal Fe accumulation is associated with fatigue, low immunity, and chronic degenerative diseases [18]. These inevitable barriers provoke an urgent need for a suitable delivery system.

In this study, we constructed a supramolecular structure based on polyphenol (tannic acid, TA) and iron ions to deliver DOC (DOC@TA-Fe^{3+}) with functions of microtubule inhibition, reactive oxygen species (ROS) generation, and GPX4 inhibition for ferroptosis/apoptosis treatment. Because of its reducibility, TA can convert Fe^{3+} into Fe^{2+} in a sustained manner to dynamically regulate the Fenton reaction activity [15,23]. The DOC@TA-Fe^{3+} nanoreactor can rapidly accumulate in mouse tumor tissues once administered through the tail vein. When the DOC@TA-Fe^{3+} nanoreactor is internalized, it depolymerizes and releases TA, Fe^{3+}, and DOC. The released TA converts Fe^{3+} into Fe^{2+} to continuously supply iron ions for ferroptosis initiation. Moreover, the released DOC from the DOC@TA-Fe^{3+} nanoreactors can control microtubule dynamics, which subsequently induces apoptosis in tumor cells. Significant antitumor therapeutic efficacy is achieved via ferroptosis and microtubule inhibition in vitro and in vivo.

2. Materials and methods

2.1. Materials

TA, $FeCl_3 \cdot 6H_2O$ and H_2O_2 were purchased from Sigma-Aldrich (St. Louis, MO, USA). DOC and calcein acetoxymethyl ester (calcein-AM)/propidium iodide (PI) detection kits were obtained from Dalian Meilun Biotech Co., Ltd. (Dalian, China). Methylene blue (MB), ethanol, hydroxylamine hydrochloride, tetrazolium (MTT) 1,10-phenanthroline monohydrate, GSH, vitamin E (VE), glutamate (Glu), cysteine (Cys), Tween 20, and phosphate buffer solution (PBS) were bought from Aladdin-Reagent Co., Ltd. (Shanghai, China). Deferoxamine mesylate (DFO), ferrostatin-1 (Fer-1), necrostain-1 (Nec-1), 3-methyladenine (3-MA), and benzyloxycarbonyl-Val-Ala-Asp(OMe)-fluoromethylketone (APO) were acquired from MedChemExpress (Monmouth Junction, NJ, USA). Chlorin e6 (Ce6) was purchased from Shanghai Yuanye Bio-Technology Co., Ltd. (Shanghai, China). Primary monoclonal antibodies (Bax, Bcl2, caspase 9, GPX4, COX2, XCT, and SLC3A2) and secondary antibodies were purchased from HuaBio (Huangzhou, China).

2.2. Preparation of DOC@TA-Fe^{3+} nanoreactor

DOC powder was dissolved in ethanol at 5, 10, and 20 mg/mL. Briefly, 10 mL of DOC solutions at different concentrations were added to 970 μL of Milli-Q water and ultrasonicated for 2 min. Afterward, 10 μL of TA solution (10, 20, 40, 60, and 80 mg/mL) and 10 μL of $FeCl_3$ solution (5, 10, 15, and 20 mg/mL) were immediately added to the above dispersion of DOC nanocores under ultrasonication. The nanoparticles were rinsed with distilled water to remove excess Fe^{3+} and TA.

2.3. Characterization

The hydrodynamic diameter of the DOC@TA-Fe^{3+} nanoreactor was measured using a dynamic laser light (DLS) (Nano-ZS 90, Malvern, UK). The morphologies of the DOC nanocores and DOC@TA-Fe^{3+} nanoreactor were detected via transmission electron microscopy (TEM; HT7800, Hitachi, Tokyo, Japan). The ultraviolet-visible (UV-Vis) spectra of TA, Fe^{3+}, and TA-Fe^{3+} were measured using UV (Shimadzu, Kyoto, Japan). The X-ray photoelectron spectroscopy (XPS) of the DOC@TA-Fe^{3+} nanoreactor was obtained via a Thermo Scientific Escalab Xi+ (Waltham, MA, USA). Details on encapsulation efficiency (EE) and drug loading (DL) assay can be found in the Supplementary data.

2.4. ·OH generation mediated by Fenton-like reaction

MB degradation was performed to detect ·OH generation. MB (25 μg/mL) and H_2O_2 (10 mM) were added to water as a control. $FeCl_3$ solution and TA-Fe^{3+} solutions containing MB and H_2O_2 were shaken for 30 min at 37 °C. UV-vis was used to analyze MB degradation.

For the examination of TA's capacity to convert Fe^{3+} into Fe^{2+}, TA-Fe^{3+} solutions with pH 7.4 and 5.6 containing MB and H_2O_2 were incubated at 37 °C for 30 min to observe the UV spectrum of MB. The ·OH generated by the Fenton-like reaction was further detected via electron spin resonance (ESR) spectroscopy (EMXplus, Saarbrucken, Germany). Only DOC@TA-Fe^{3+} nanoreactor was arranged as a control. Briefly, 100 μL of DOC@TA-Fe^{3+} + H_2O_2 (pH 7.4) and DOC@TA-Fe^{3+} + H_2O_2 (pH 5.6) solution were added to 5,5-dimethyl-1-pyrroline N-oxide buffer solution. After incubation for 15 min, X band EPR spectra were detected.

2.5. In vitro drug release behavior

To evaluate the drug release from free DOC and DOC@TA-Fe^{3+} nanoreactor, a dialysis method was used. Dialysis bags were filled with 1 mL of free DOC or DOC@TA-Fe^{3+} (molecular weight cut-off: 1000 Da) and submerged in 10 mL of PBS (pH 5.6 and 7.4) with 0.05% (V/V) Tween 20. The beakers were placed in a shaker. Briefly, 2 mL of dialysate was collected, and the fresh buffer was added at a specific time. The released DOC was monitored using high-performance liquid chromatography (Waters E2695, Milford, MA, USA).

A standard curve was established to assay the release behavior of iron ions. The content of Fe^{3+} in the DOC@TA-Fe^{3+} nanoparticles was detected. Briefly, 1 mL of DOC@TA-Fe^{3+} solution was placed in a dialysis bag, which was immersed in 10 mL of PBS (pH 5.6 and 7.4) and then placed in a shaker at 37 °C and 100 r/min. Afterward, 1 mL of the solution was collected and supplied with the same volume of fresh solution at different time points. Hydroxylamine hydrochloride was added to the above solution and incubated for 15 min. Finally, 1,10-phenanthroline (1 mg/mL) was provided to react with the mixed solution and measured at 510 nm [24].

2.6. Colocalization of DOC@TA-Fe^{3+}

CT26 cells were seeded onto confocal dishes and cultured overnight. A fresh medium containing Ce6-doped DOC@TA-Fe^{3+} was added and incubated for 2, 4, 6, and 8 h. The cells were stained with Hoechst 33342 and Lysotracker green (Beyotime, Shanghai, China) for 10 and 20 min, respectively. Finally, colocalization was investigated via confocal laser scanning microscopy (CLSM; Zeiss LSM880, Oberkochen, Baden-Wurttemberg, Germany). The methods of cell culture, cell uptake, and cell cycle assay are shown in the Supplementary data.

2.7. Cell cytotoxicity

Briefly, 3×10^3 CT26 cells were seeded into 96-well plates, incubated for 12 h, added with free DOC, DOC@TA-Fe^{3+}, and DOC@TA-Fe^{3+} + DFO at various concentrations, and incubated for another 24 h. Afterward, 20 μL of MTT (5 mg/mL) was added to the cells for 4 h, and absorbance was detected using a microplate reader (BioTek, Winooski, VT, USA).

The DOC@TA-Fe^{3+} solution was added to the 96-well plate with CT26 cells. After incubation for 2 h, ferroptosis inhibitors and activators (namely, Fer-1, GSH, VE, DFO, Glu, and Cys), a necroptosis inhibitor (necrostain-1), an autophagy inhibitor (3-MA), and an apoptosis inhibitor (APO) were added to the DOC@TA-Fe^{3+}-treated cells for 24 h. Finally, MTT was added for tumor cell viability assay.

2.8. Cell apoptosis

Annexin V-fluorescein isothiocyanate (FITC)/7-amino-actino-mycin D (7AAD) kit (BD Biosciences, NJ, USA) was used to track CT26 cell apoptosis. The CT26 cells were treated with Fe^{3+}, TA-Fe^{3+}, DOC, DOC@TA-Fe^{3+}, and DOC@TA-Fe^{3+} + DFO. After incubation for 24 h, the cells were collected by adding free ethylenediaminetetraacetic tyrisin and incubated with the Annexin V-FITC/7AAD detection kit. Finally, the cell apoptosis ratio was analyzed via flow cytometry (ACEA Pharma, San Diego, CA, USA).

The CT26 cells were plated in plates to further visualize the live and dead cells after treatment with Fe^{3+}, TA-Fe^{3+}, DOC, DOC@TA-Fe^{3+}, and DOC@TA-Fe^{3+} + DFO. After treatment for 24 h, the cells were coincubated with calcein-AM and PI for 30 min in the dark to observe with CLSM.

2.9. Western blot (WB) assay

CT26 cells were treated with $FeCl_3$, DOC, TA-Fe^{3+}, DOC@TA-Fe^{3+}, and DOC@TA-Fe^{3+} + DFO for 24 h, collected, and washed with cold PBS. The cells were then lysed and sonicated with radio-immunoprecipitation assay lysis buffer in an ice bath. The supernatants containing protein were obtained via centrifugation at 4 °C. Protein concentration was detected using a bicinchonininc acid kit (Biosharp Life Sciences, Hefei, China). The supernatants were mixed with loading buffer to boil for 10 min. Sodium dodecyl sulfate-polyacrylamide gel electrophoresis was used to determine protein expression. The proteins were then transferred to 0.45-μm poly-vinylidene fluoride membranes, treated with primary monoclonal antibodies (1:2000; Bax, Bcl2, caspase 9, GPX4, COX2, XCT, and SLC3A2), and incubated with horseradish peroxidase-coupled secondary antibody for observation.

2.10. Intracellular ·OH assay

With the aid of ROS, 2,7-dichlorodihydrofluorescein diacetate (DCFH-DA) (Beyotime, Shanghai, China) could be oxidized to DCF with a green fluorescence signal. Thus, DCFH-DA was chosen for the assay of intracellular ·OH generation. CT26 cells seeded in 24-well plates were treated with Fe^{3+} (30 μg/mL), TA-Fe^{3+}, DOC, DOC@TA-Fe^{3+}, and DOC@TA-Fe^{3+} + DFO. After incubation for 4 h, DCFH-DA solution (10 μM) was added to the stain for 30 min in the dark. Finally, the fluorescence images were observed with Apotome microscopy (Zeiss Company, Oberkochen, Baden-Wurttemberg, Germany). The cells were collected for flow cytometry assay.

2.11. Immunofluorescent staining

CT26 cells were incubated with $FeCl_3$, TA-Fe^{3+}, DOC, DOC@TA-Fe^{3+}, and DOC@TA-Fe^{3+} + DFO. After incubation for 24 h, the cells were fixed with 4% paraformaldehyde (Servicebio, Wuhan, China) for 20 min, permeabilized with 0.1% Triton-100 (Sigma-Aldrich, St. Louis, MO, USA) for 20 min, and sealed with 1% bovine serum albumin (Aladdin) for 1 h. The cells were then treated with anti-tubulin antibodies (1:150; HuaBio), incubated with goat antirabbit secondary antibody (HuaBio) for 2 h, and stained with 4′,6-diamidino-2-phenylindole (Aladdin). Finally, the cells were observed with CLSM.

2.12. In vivo fluorescence imaging

Female BALB/c mice (7−8 weeks) were obtained from Beijing HFK Bioscience Co., Ltd. (Beijing, China). All animal experiments were approved by the Animal Ethics Committee of West China

Hospital of Sichuan University (Chengdu, China) and conducted in accordance with the Guidelines for Care and Use of Laboratory Animals of Sichuan University (Approval No: 20211055 A).

Tumor-bearing mice were established by subcutaneously injecting 1×10^6 CT26 cells in 100 μL of serum-free 1640 medium. The mice were used for in vivo imaging when the tumor volume reached 100 mm^3 Ce6-labeled DOC@TA-Fe^{3+} in PBS solution (200 μL) was intravenously injected into CT26-bearing mice (Ce6: 3.5 mg/kg). Fluorescence images were captured at 1, 3, 6, and 12 h using an IVIS in vivo imaging instrument (PerkinElmer, Waltham, MA, USA).

2.13. In vivo efficacy study

Once the tumor volume reached 100 mm^3, the tumor-bearing mice were randomly divided into six groups and intravenously injected with normal saline (NS), $FeCl_3$, TA-Fe^{3+}, DOC, DOC@TA-Fe^{3+}, and DOC@TA-Fe^{3+} + DFO solutions three times a day every two days (DOC: 10 mg/kg; $FeCl_3$: 3.5 mg/kg). DFO was also administered via intraperitoneal injection (10 mg/kg). Finally, the tumors and major organs were collected and stained with hematoxylin and eosin staining (H&E) for histological examination. The tumors were used to determine the expressions of CD31 and Ki67 (Servicebio, Wuhan, China). CT26 in-situ tumor-bearing mice were also used to evaluate the therapeutic effect of the nanoreactor.

2.14. Statistical analysis

Student's *t*-test and one-way analysis were used to evaluate the differences and determine the significance of the efficacy studies. Data were expressed as mean ± standard deviation.

3. Results and discussion

3.1. Preparation and characterization of DOC@TA-Fe^{3+}

Polyphenols, which have biological activities including anti-tumor, antioxidation, and antiradiation activities, are widely present in tea, fruits, and vegetables. The catechol hydroxyl of polyphenols can coordinate with multivalent metal ions without the help of special solvents. Because of the rapid, simple, and green preparation and the simultaneous introduction of one or more metal ions, metal-polyphenol supramolecular complexes are being used for drug delivery, biological imaging, and catalysis. The metal ions of the metal-polyphenol structure can induce ferroptosis in tumor cells [15,17]. In this study, nanoscale metal-polyphenol supermolecules possessing DOC nanocores (DOC@TA-Fe^{3+}) were fabricated via a reported co-ordination method [23]. The size of the prepared various DOC@TA-Fe^{3+} supermolecules was measured using DLS. The morphology of the DOC nanocore and DOC@TA-Fe^{3+} was observed via TEM (Fig. 1A). TEM revealed the typical network structure of DOC@TA-Fe^{3+} formed because of the coordination between Fe^{3+} and TA. A series of nanoreactors with different concentrations of TA and Fe^{3+} were prepared, and the size of these DOC@TA-Fe^{3+} nanoreactors was measured using DLS (Fig. S1). The concentration of Fe^{3+} (10 mg/mL) was fixed, and the EE and DL of DOC were measured at various TA concentrations (Table S1). The stability of these nanoreactors was also measured using DLS (Fig. S2). The results suggested that the nanoreactor (Fe^{3+}: 10 mg/mL; TA: 40 mg/mL) showed great stability. Additionally, the size of the other nanoreactors with different TA concentrations started to improve with time. Based on the analysis of DL and stability, DOC@TA-Fe^{3+} (Fe^{3+}: 10 mg/mL; TA: 40 mg/mL) was used for a subsequent experiment. The element species of DOC@TA-Fe^{3+} was investigated via XPS (Fig. 1B). The spectrum of iron displayed three main peaks at 712.6, 715.4, and 725.8 eV

(Fig. S3), which were attributed to $Fe^{3+}2p_{3/2}$, $Fe^{3+}2p_{3/2}$ satellite, and $Fe^{3+}2p_{1/2}$, respectively [25–28]. As shown in Fig. 1C, the UV-vis absorption spectrum of the DOC@TA-Fe^{3+} nanoreactor displayed a broad peak at 560 nm, which was caused by the coordination complexation between the metal and phenol and indicated the formation of a metal-phenolic supermolecule [29,30]. Given that the efficiency of ferroptosis is dependent on the Fenton reaction, MB was used to evaluate the occurrence of the Fenton reaction [25,31]. The absorbance of MB in the TA-Fe^{3+} reaction systems (pH 7.4 and 5.6) declined (Figs. 1D and S4) compared with that in the MB-only group, indicating that ·OH was generated. Particularly, the absorbance of MB decreased with the increased acidity because the supramolecular structure of metal-polyphenols is pH-responsive [32,33]. TEM images of DOC@TA-Fe^{3+} nanoreactor with acidic incubation showed that the nanoreactors were depolymerized (Fig. S5). When the acidity increased, metal-phenol depolymerization was intensified, leading to an increase in the amount of iron ions participating in the Fenton reaction. Additionally, accelerating the transformation of Fe^{3+} to Fe^{2+} in a sustained manner is a simple and efficient method to dynamically regulate the Fenton reaction

activity. Because of its high reduction property, TA can convert Fe^{3+} into Fe^{2+} to improve the efficiency of the Fenton reaction under acidic conditions [23,34]. As shown in Fig. S6, ESR spectroscopy was used to further detect ·OH. Compared with that of the only DOC@TA-Fe^{3+} group, the ESR signal of the DOC@TA-Fe^{3+} + H_2O_2 reaction system was enhanced. Additionally, the ESR signal of DOC@TA-Fe^{3+} + H_2O_2 was further improved after pH adjustment. This trend was consistent with the above results from the MB assay. The realization of ferroptosis with the as-prepared nanoreactor essentially depends on the efficient release of Fe^{3+} from the DOC@TA-Fe^{3+} nanoreactor. Therefore, the acid-induced dissociation behavior of the nanoreactor was measured. As shown in Figs. 1E and F, Fe^{3+} and DOC were not released at pH 7.4. Conversely, DOC@TA-Fe^{3+} displayed a fast DOC and Fe^{3+} release rate in the acidic medium (pH 5.6).

3.2. Cellular uptake

As shown in the results of CLSM and flow cytometry analysis in Fig. S7, the fluorescence signal of CT26 cells pretreated with free Ce6
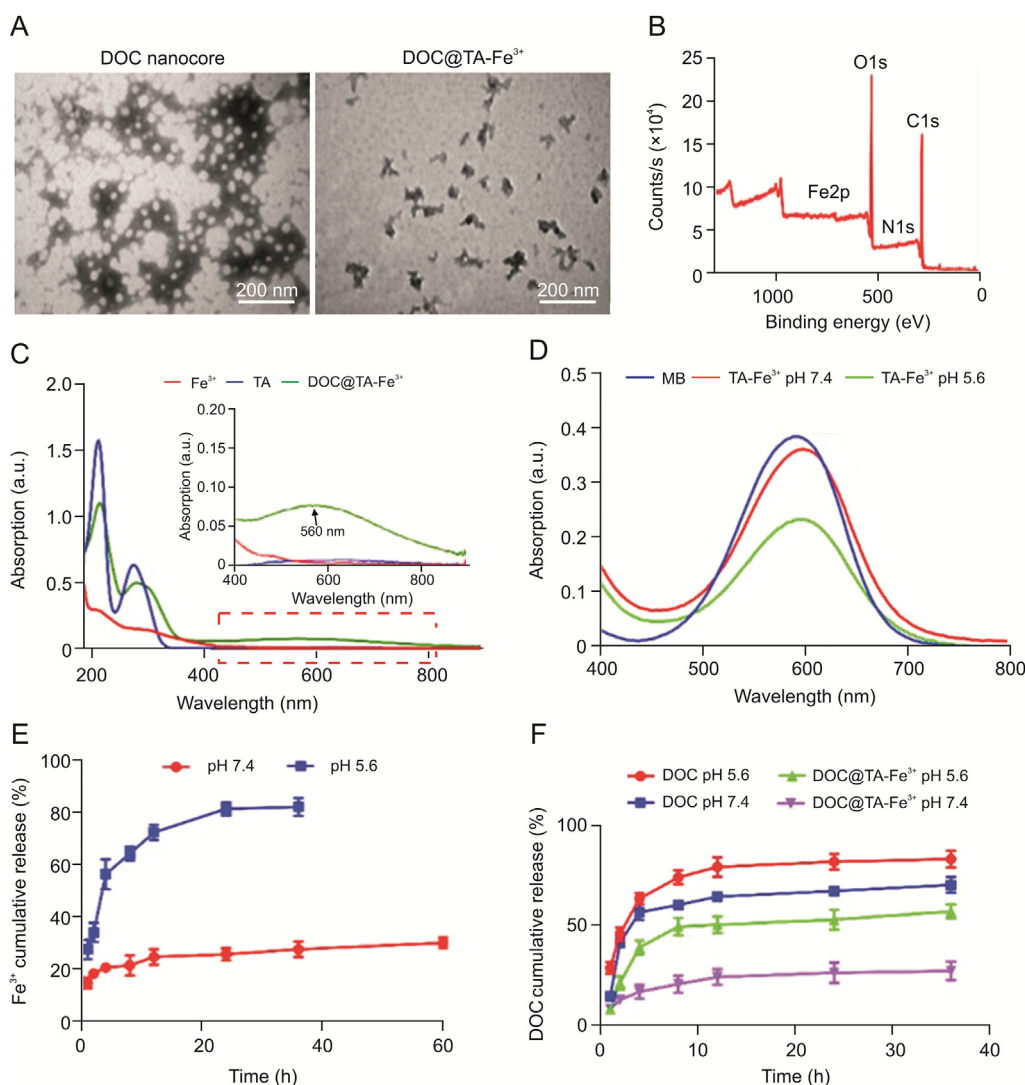

Fig. 1. Physicochemical characterization of docetaxel (DOC)@tannic acid (TA)-Fe^{3+} nanoreactors. (A) Transmission electron microscopy (TEM) images of DOC nanocore and DOC@TA-Fe^{3+} nanoreactors. (B) X-ray photoelectron spectroscopy (XPS) pattern of DOC@TA-Fe^{3+}. (C) Ultraviolet-visible (UV-Vis) absorption spectra of $FeCl_3$, TA, and DOC@TA-Fe^{3+}. Inset: The absorption of Fe^{3+}, TA, and DOC@TA-Fe^{3+} solutions within 400−800 nm. (D) Methylene blue (MB) degradation of TA-Fe^{3+} solutions in the presence of H_2O_2 at pH 5.6 and 7.4. (E) Fe^{3+} and (F) DOC release from DOC@TA-Fe^{3+} at pH 5.6 and 7.4.
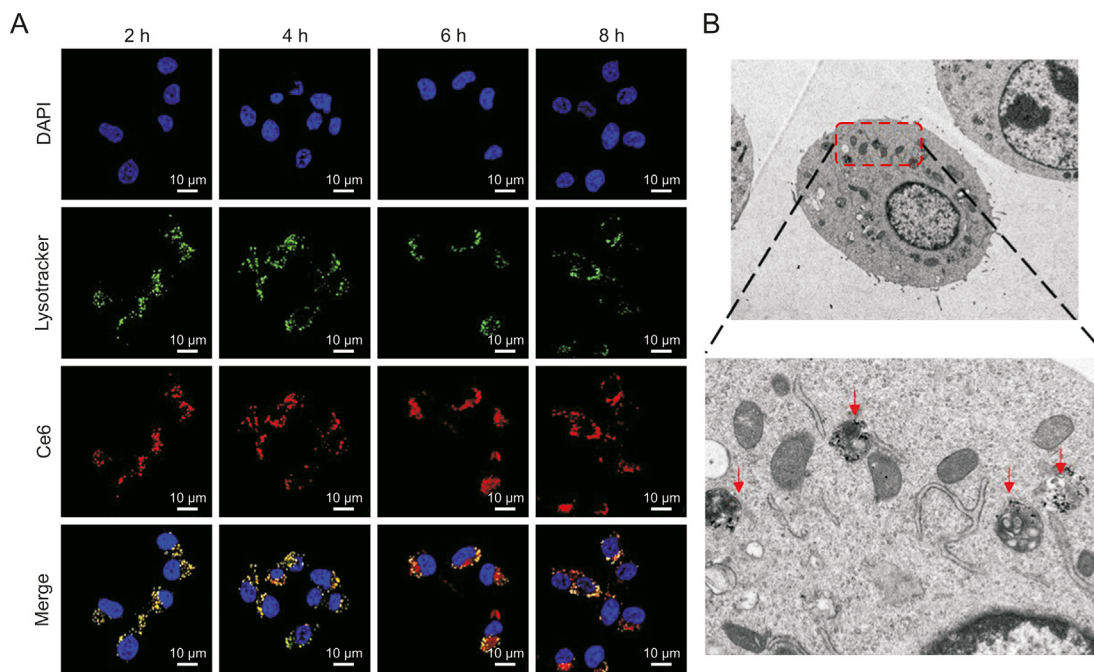
Fig. 2. The lysosome escape of docetaxel (DOC)@tannic acid (TA)-Fe^{3+} nanoreactors assay. (A) Lysosome escape of DOC@TA-Fe^{3+} in CT26 cells via confocal laser scanning microscopy. (B) Morphology of CT26 cells treated with DOC@TA-Fe^{3+} nanoreactors. The image below is a partial enlargement of the image above. The red arrows refer to DOC@TA-Fe^{3+} nanoreactors. DAPI: 4′,6-diamidino-2-phenylindole; Ce6: chlorin e6.
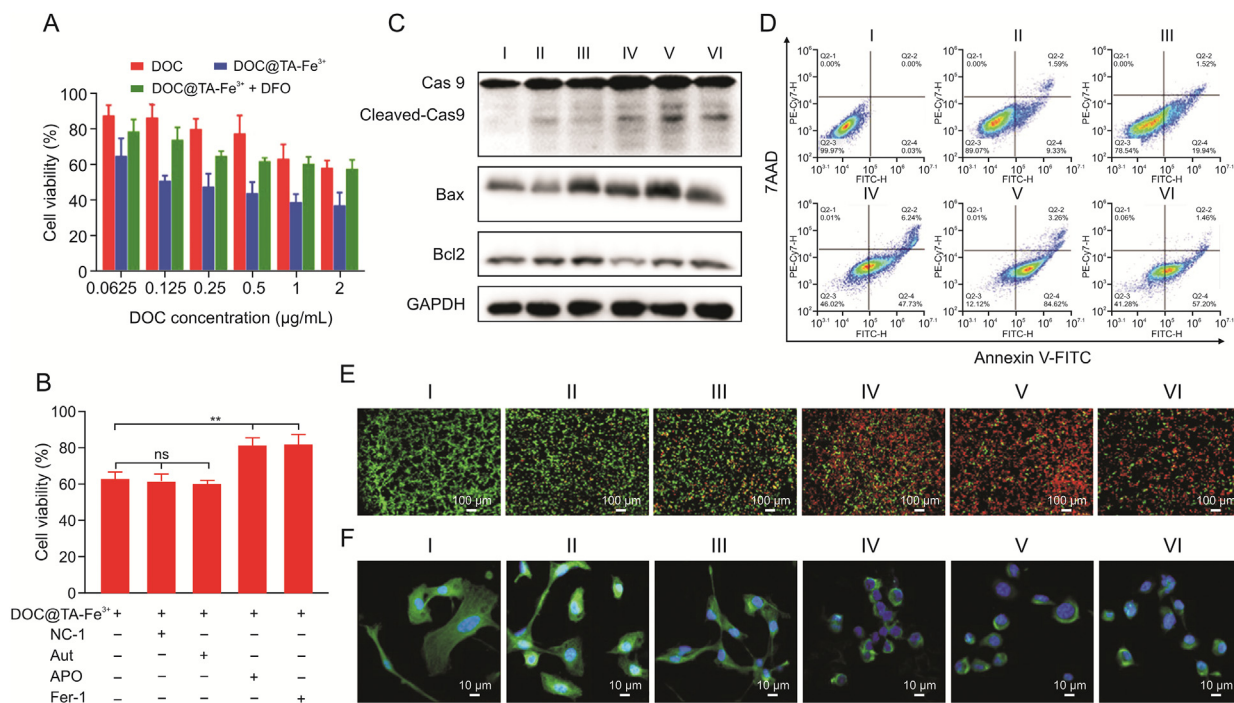

Fig. 3. The cell cytotoxicity of the docetaxel (DOC)-based nanoreactors. (A) Cytotoxicity of CT26 cells after treatment with DOC, DOC@tannic acid (TA)-Fe^{3+}, and DOC@TA-Fe^{3+} + deferoxamine mesylate (DFO) for 24 h. (B) Cell viability of CT26 cell coincubated with DOC@TA-Fe^{3+} and necrostain-1 (NC-1), 3-methyladenine (3-MA) (Aut), benzyloxycarbonyl-Val-Ala-Asp(OMe)-fluoromethylketone (APO), and ferrostatin-1 (Fer-1) for 24 h. (C) Western blot analysis of caspase 9 (Cas 9), Bax, and Bcl2 expressions in CT26 cells posttreatment with different formulations. (D) Annexin V- fluorescein isothiocyanate (FITC)/7-amino-actinomycin D (7AAD) analysis of CT26 cells treated with different formulations for 24 h via flow cytometry. (E) Fluorescent images of CT26 cells stained by calcein acetoxymethyl ester (calcein-AM) (live cells) and propidium iodide (PI) (dead cells) after treatment. (F) Microtubule imaging in CT26 cells treated by the different formulations. I: normal saline (NS); II: FeCl$_3$; III: TA-Fe^{3+}; IV: DOC; V: DOC@TA-Fe^{3+}; VI: DOC@TA-Fe^{3+} + DFO. GAPDH: glyceraldehyde-3-phosphate dehydrogenase. $^{**}P<0.01$; ns: no difference.

and the Ce6/DOC@TA-Fe^{3+} nanoreactor was enhanced with time, suggesting the successful internalization into the CT26 cells. The fluorescence intensity of Ce6 was higher than that of Ce6/DOC@TA-Fe^{3+} possibly because of the passive diffusion of Ce6 (a small molecule). The efficient intracellular delivery of the nanoreactor and release of therapeutic payloads are important issues in tumor therapy. However, after internalization, Ce6/DOC@TA-Fe^{3+} is sequestered in cellular lysosomes to reduce the therapeutic bioavailability, leading to poor therapeutic outcomes. Thus, lysosomal escape has been considered as a critical "bottleneck" for on-demand intracellular delivery [35,36]. Colocalization analysis of Ce6/DOC@TA-Fe^{3+} in CT26 cells was conducted via CLSM. The DOC@TA-Fe^{3+} nanoreactors were phagocytized by CT26 cells (Fig. 2A). After 2 h of incubation, the red signal of the nanoreactor overlapped with the yellow signal of lysosomes, and an enhanced yellow signal was found inside the cells at 4 h. Some nanoreactors escaped from the lysosomes when the incubation time was prolonged. This phenomenon is attributed to

the TA-Fe^{3+} complexation state changing from tris to bis, enabling the disruption of lysosomal membranes [36]. The pH-responsive multivalent coordination endowed the metal-polyphenol with a pH-buffering capacity [36]. The TEM images of the cells revealed the cellular uptake of DOC@TA-Fe^{3+} and the disruption of lysosomal membranes (Fig. 2B).

3.3. Mechanism underlying DOC@TA-Fe^{3+}-induced cell death

The nanoreactor can be efficiently taken up and escape from lysosomes. Next, its antitumor efficacy was examined. In the MTT assay, the DOC, DOC@TA-Fe^{3+}, and DOC@TA-Fe^{3+} + DFO groups presented dose-dependent cytotoxicity (Fig. 3A). Compared with free DOC and DOC@TA-Fe^{3+} + DFO, DOC@TA-Fe^{3+} effectively enhanced the cytotoxicity because of the synergistic effects of apoptosis and ferroptosis. Additionally, polyphenol exhibits antitumor effects in several cancers, thus promoting the cytotoxicity of
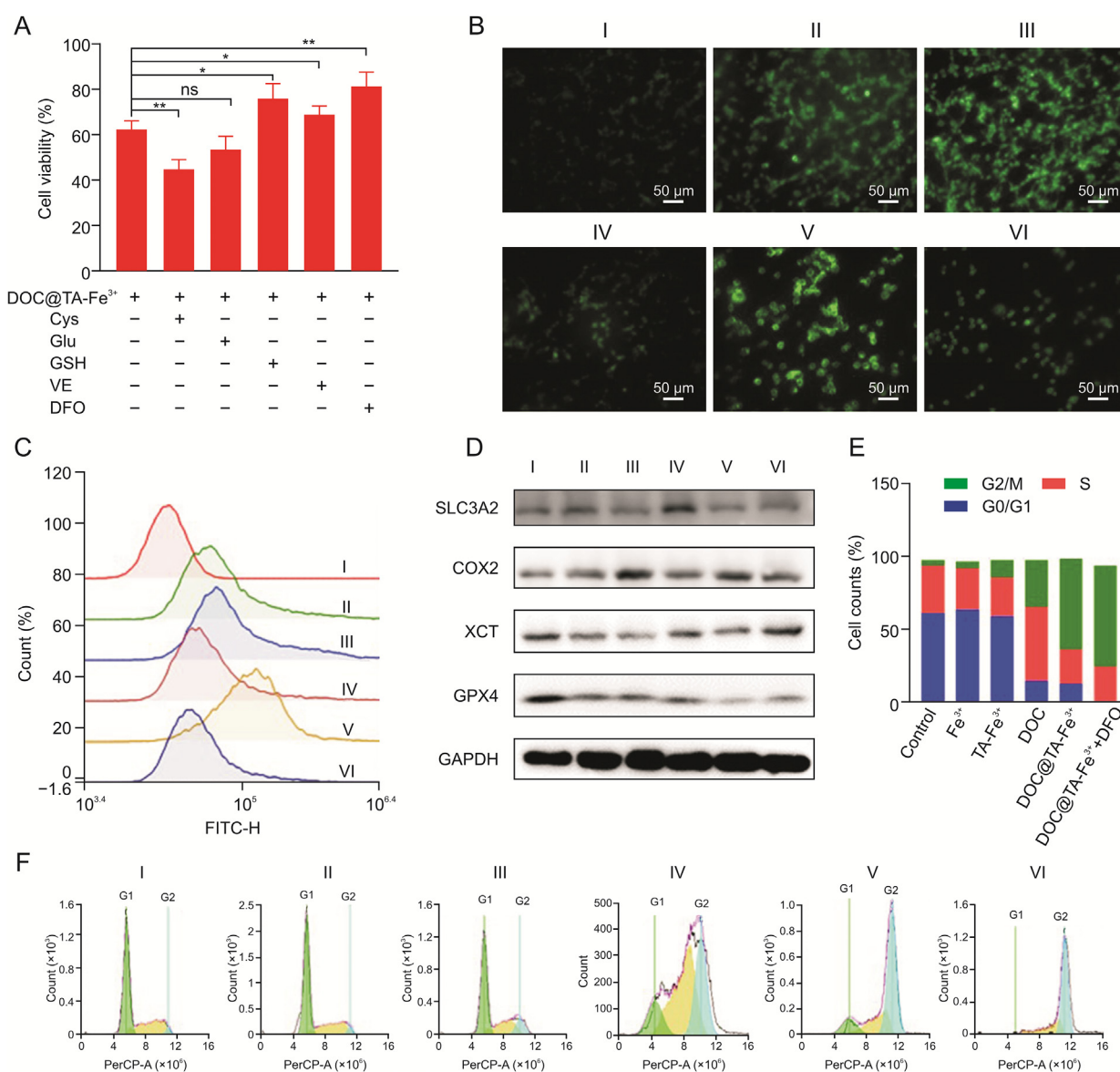

Fig. 4. The ferroptoris mechanism of docetaxel (DOC)@tannic acid (TA)-Fe^{3+}. (A) Effect of ferroptosis inhibitors and activators on the cytotoxicity of DOC@TA-Fe^{3+}. (B) Fluorescence images and (C) flow cytometry assay of reactive oxygen species in CT26 cells detected via 2,7-dichlorodihydrofluorescein diacetate staining after different treatments. (D) Ferroptosis-related protein activity of CT26 cells after different stimulations. (E, F) Cell cycle of CT26 cells after being treated with different formulations. I: normal saline (NS); II: FeCl$_3$; III: TA-Fe^{3+}; IV: DOC; V: DOC@TA-Fe^{3+}; VI: DOC@TA-Fe^{3+} + DFO. GSH: glutathione; VE: vitamin E; Glu: glutamate; Cys: cysteine; DFO: deferoxamine mesylate; FITC: fluorescein isothiocyanate.
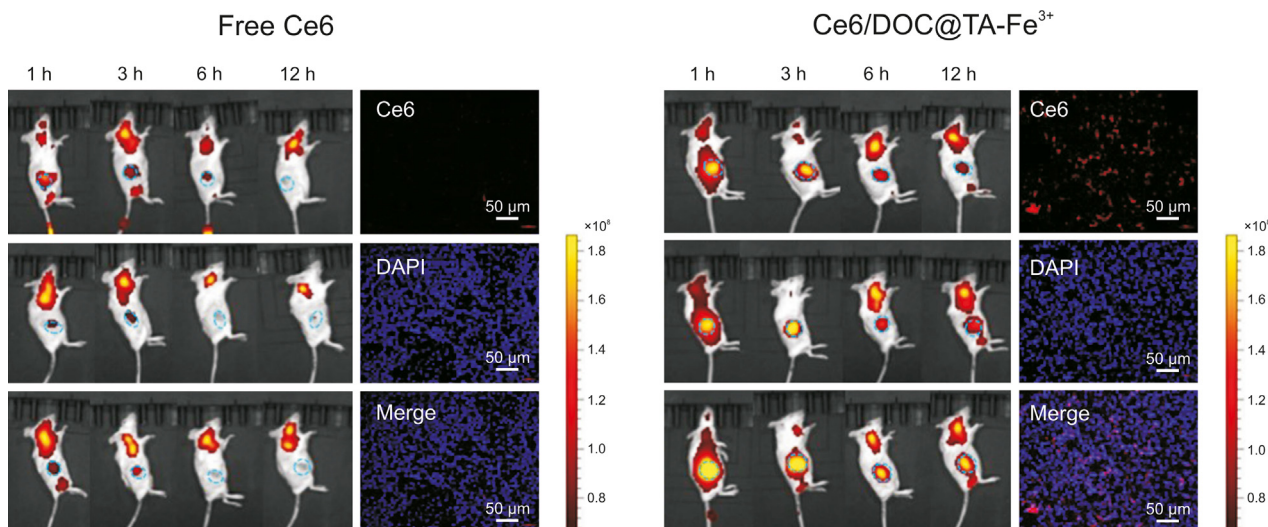
Free Ce6

Ce6/DOC@TA-Fe^{3+}

Fig. 5. Tumor targeting and retention behaviors of chlorin e6 (Ce6)/docetaxel (DOC)@tannic acid (TA)-Fe^{3+}. The in vivo fluorescence images of CT26 tumor-bearing mice intravenous injection with Ce6-labeled DOC@TA-Fe^{3+} at different time intervals. The tumor section after 12 h of administration was stained with 4′,6-diamidino-2-phenylindole (DAPI) to observe the DOC@TA-Fe^{3+} distribution.

chemotherapy [37,38]. L929 cells were used to evaluate the cytotoxicity of DOC@ TA-Fe^{3+} against normal cells (Fig. S8). The cytotoxicity of the DOC@ TA-Fe^{3+} nanoreactors to normal cells was significantly lower than that of CT26 tumor cells.

To verify the mechanism of cell death, some inhibitors related to cell death pathways were applied. Fer-1 and APO could remarkably alleviate the cell viability induced by DOC@TA-Fe^{3+}, and 3-MA and necrostain-1 could not rescue the cell from death (Fig. 3B). Thus, we speculated that ferroptosis and apoptosis pathways are involved in the cell death induced by DOC@TA-Fe^{3+}. The above results indicated that apoptosis is another mechanism of DOC@TA-Fe^{3+}-induced cell death. The expressions of caspase 9, Bax, and Bcl$_2$ in
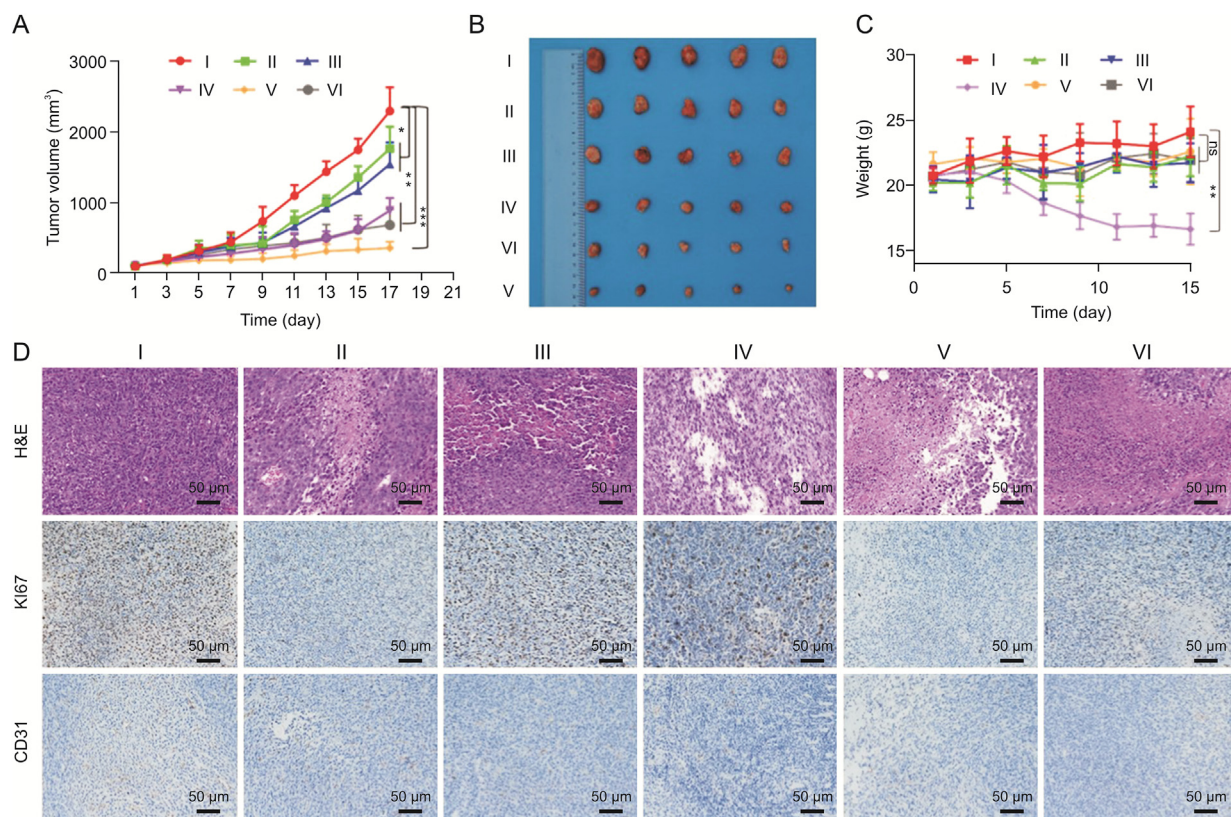

Fig. 6. In vivo tumor therapeutics of docetaxel (DOC)@tannic acid (TA)-Fe^{3+} nanoreactors by intravenous injection. (A) Tumor volume after phosphate buffer solution and DOC-loaded nanoreactors ($n = 5$). (B) Photos of the tumors after intravenous treatments (day 10). (C) Body weight changes of the mice. (D) Hematoxylin-eosin staining (H&E) and immunohistochemical analysis of CD31 and KI67. I: normal saline (NS); II: FeCl$_3$; III: TA-Fe^{3+}; IV: DOC; V: DOC@TA-Fe^{3+}; VI: DOC@TA-Fe^{3+} + deferoxamine mesylate (DFO). *$P <$ 0.05, **$P <$ 0.01, ***$P <$ 0.005; ns: no significance.

CT26 cells after different treatments were analyzed to further determine the apoptosis mechanism (Figs. 3C and S9). The results showed that Fe^{3+} and $TA-Fe^{3+}$ did not affect the transcription and translation of apoptosis proteins. In fact, DOC, DOC@TA-Fe^{3+}, and DOC@TA-Fe^{3+} + DFO promoted the apoptosis of the CT26 cells. Apoptosis ratios were analyzed via flow cytometry using Annexin V-FITC and 7AAD. Fig. 3D shows that the cell apoptosis ratio was significantly increased after treatment with DOC, DOC@TA-Fe^{3+}, and DOC@TA-Fe^{3+} + DFO. DFO cotreatment led to ferroptosis diminishment as a result of iron ion chelation [23]. The cell apoptosis ratio of the DOC@TA-Fe^{3+} group was higher than that of the DOC and DOC@TA-Fe^{3+} + DFO groups. This phenomenon occurred because ferroptosis improves cell sensitivity to apoptosis, thus enhancing the antitumor effect [39,40]. Fig. 3E also shows an enhanced PI fluorescence signal from the CT26 cells after treatment with DOC-loaded nanoreactors compared with that of control, $FeCl_3$, and $TA-Fe^{3+}$ groups via calcein-AM/PI staining. These results were similar to the cytotoxicity findings.

DOC@TA-Fe^{3+} initiates ferroptosis and acts on microtubules, eventually leading to apoptosis. In contrast to the control group, the DOC-loaded nanoreactors generally triggered the destruction of microtubules and the loss of filamentous networks (Fig. 3F).

Because of the presence of Fe^{3+} in the DOC@TA-Fe^{3+} nanoreactors, tumor cell death after treatment with DOC@TA-Fe^{3+} depends on control microtubules and iron ions. Ferroptosis inhibitors and activators were introduced for cell viability assay to investigate the mechanism of ferroptosis [36,41] (Fig. 4A). The addition of Cys and Glu (ferroptosis activators) enhanced the cytotoxicity and decreased the cell viability in response to DOC@TA-Fe^{3+}. GSH, VE (a liposoluble antioxidant), and DFO (iron-chelating agent) could relieve the cytotoxicity of DOC@TA-Fe^{3+}, indicating the occurrence of ferroptosis [23,42,43].

ROS accumulation plays an important role in the induction of ferroptosis. We observed that Fe^{3+}, $TA-Fe^{3+}$, and DOC@TA-Fe^{3+} significantly increased ROS generation in CT26 cells (Figs. 4B and C). As a reducing agent in the DOC@TA-Fe^{3+} nanoreactors, TA may convert Fe^{3+} into Fe^{2+} with high catalytic activity for the Fenton reaction. Thus, the fluorescence intensity of $TA-Fe^{3+}$ is higher than that of Fe^{3+}. Compared with that in the DOC@TA-Fe^{3+} group, ROS generation in the DOC@TA-Fe^{3+} + DFO group was lower because DFO is an iron chelator that can react with Fe^{3+} to inhibit the Fenton reaction.

xCT, which mediates cysteine uptake and glutamate release, plays an important role in intracellular cysteine balance and GSH biosynthesis. GPX4 activity is the pivotal factor in ferroptosis.
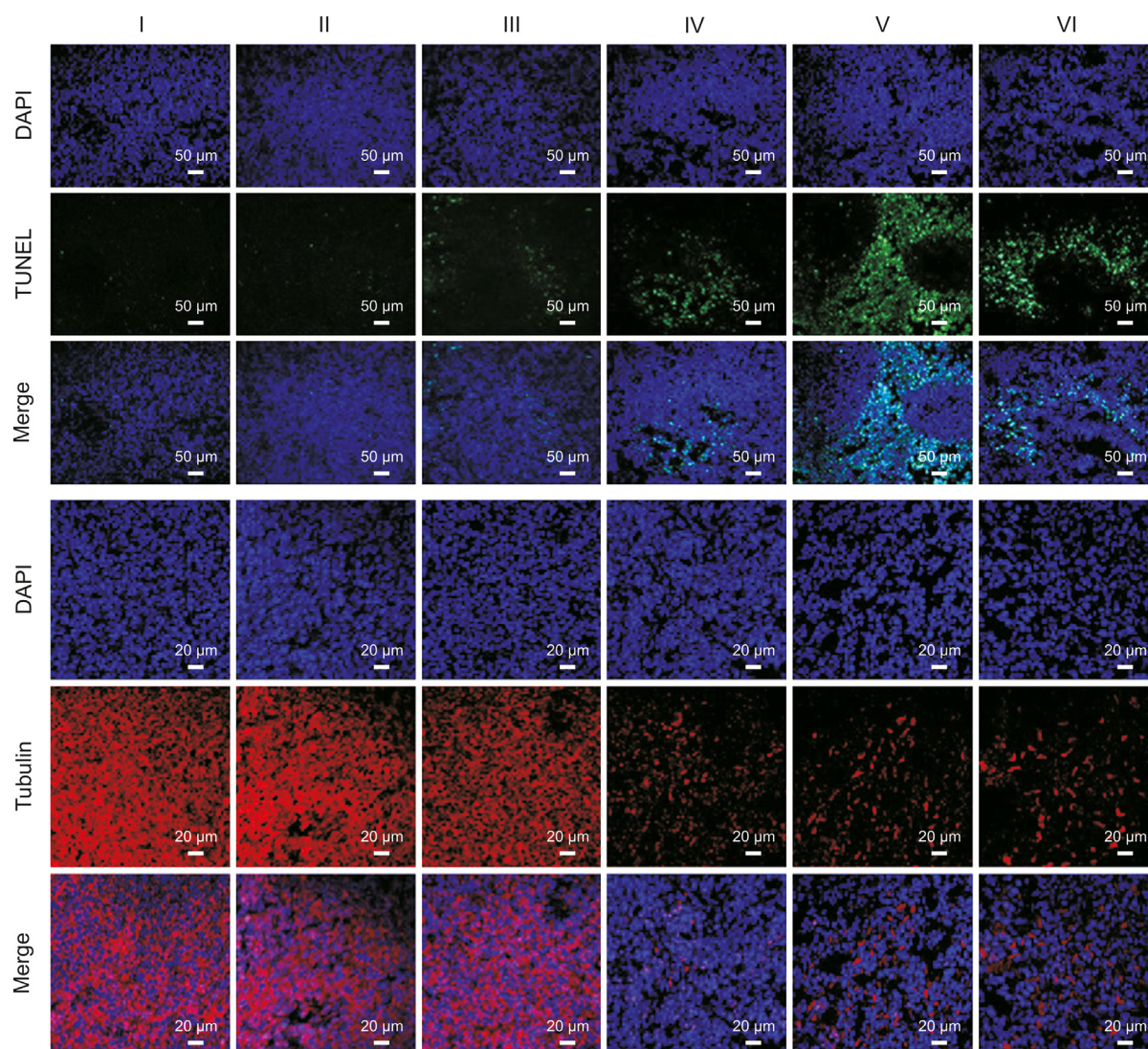

Fig. 7. The terminal dexynucleotidyl transferase (TdT)-mediated dUTP nick-end labeling (TUNEL) and tubulin staining on the dissected tumor tissues. I: normal saline (NS); II: $FeCl_3$; III: tannic acid (TA)-Fe^{3+}; IV: docetaxel (DOC); V: DOC@TA-Fe^{3+}; VI: DOC@TA-Fe^{3+} + deferoxamine mesylate (DFO). DAPI: 4′,6-diamidino-2-phenylindole.

Similarly, COX2 upregulation is a marker of ferroptosis. Therefore, WB was performed to determine the expressions of xCT, GPX4, and COX2 after treatment with different formulas. Compared with those in the control or free DOC group, the proteins of xCT and GPX4 showed reduced expression after the CT26 cells were treated with $FeCl_3$, TA-Fe^{3+}, and DOC@TA-Fe^{3+}. This finding indicated the occurrence of ferroptosis (Figs. 4D and S10). The protein levels of xCT and GPX4 were upregulated after treatment with DOC@TA-Fe^{3+} + DFO, indicating that Fe^{3+} was involved in inducing ferroptosis. Moreover, the protein levels of COX2 were upregulated when the CT26 cells were treated with an iron-based agent compared with those in the control. These results supported the DOC@TA-Fe^{3+} nanoreactor-induced ferroptosis.

After treatment with DOC@TA-Fe^{3+}, CT26 displayed the redistribution of cell cycle phases (Figs. 4E and F). The results showed that DOC-based therapy decreased the percentage of cells in the G_0/G_1 phase. A possible reason is that DOC controls the microtubule dynamics, leading to G_2/M phase arrest.

3.4. Biodistribution of DOC@TA-Fe^{3+} nanoreactors

To evaluate the distribution of DOC@TA-Fe^{3+} in vivo, a CT26 tumor-bearing mouse model was established (Fig. 5). Ce6/DOC@TA-Fe^{3+} nanoreactors were formed by loading Ce6 into DOC@TA-Fe^{3+}. The accumulated red fluorescence signal was observed at different times after the intravenous injection of Ce6-doped nanoreactors. The fluorescence intensity of the Ce6-doped

nanoreactors at the tumor site reached a maximum within 1 h. The fluorescence gradually decreased over time and was distributed throughout the body. After 12 h, the fluorescence signal was retained at the tumor site, indicating the long retention of the nanoreactors. Compared with that of the Ce6-doped nanoreactor group, the fluorescence signal of the free Ce6 group was weakened at the tumor site and accumulated in the major organs. The major organs and tumors were collected after 12 h for ex vivo imaging (Fig. S11). The fluorescence of the Ce6-doped nanoreactors was retained in the tumor site. The fluorescent signal in the liver was due to the liver metabolism of the nanoreactors. These results showed that Ce6-doped nanoreactors preferentially settle in the tumor site, which benefits the passive targeting of the nanoreactors. Additionally, the negative charge of the Ce6-doped nanoreactors is conducive to avoiding clearance by the mononuclear phagocyte system [25].

3.5. Therapeutic effect on colon cancer

After establishing the in vivo tumor accumulation of the nanoparticles, we evaluated the therapeutic effect of DOC-loaded nanoreactors against colon cancer. The tumor volume displayed a significant difference after treatment with different formulations (Fig. 6A), including NS, Fe^{3+}, TA-Fe^{3+}, DOC, DOC@TA-Fe^{3+}, and DOC@TA-Fe^{3+} + DFO. Fe^{3+} and TA-Fe^{3+} weakly suppressed tumor growth compared with that in NS because of ferroptosis induced by iron ions. The high tumor-inhibiting efficiency of
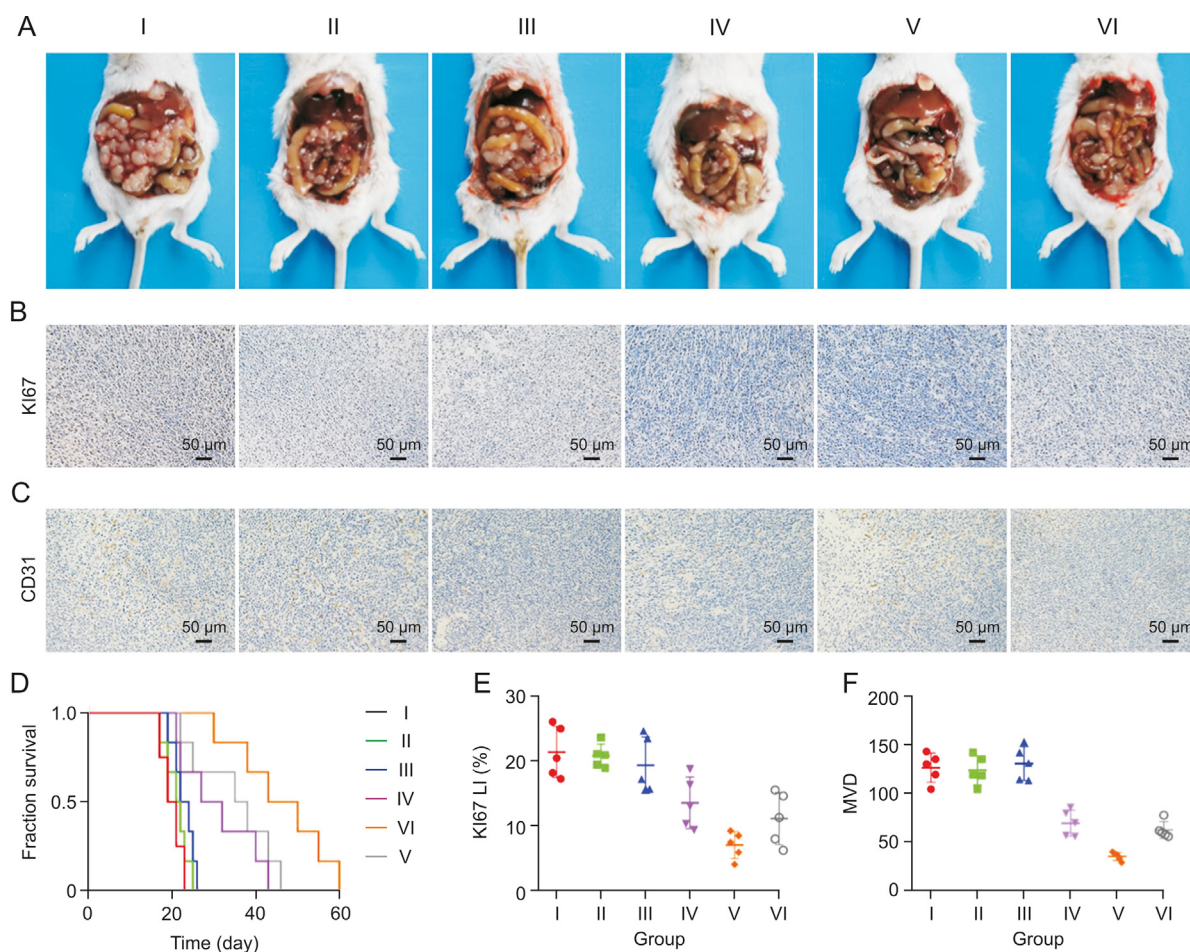

Fig. 8. The antitumor efficacy in orthotopic tumor models. (A) Representative photographs of tumor in each group. (B) KI67 and (C) CD31 immunohistochemical staining of tumor slices. (D) Survival curves of mice given different treatments. (E) Mean KI67 LI and (F) microvessel density (MVD) in each group. I: normal saline (NS); II: $FeCl_3$; III: tannic acid (TA)-Fe^{3+}; IV: docetaxel (DOC); V: DOC@TA-Fe^{3+}; VI: DOC@TA-Fe^{3+} + deferoxamine mesylate (DFO).

DOC@TA-Fe^{3+} was primarily attributed to the synergy between microtubule inhibition and ferroptosis. The addition of DFO decreased the tumor-inhibiting potency of DOC@TA-Fe^{3+} as a result of iron ion removal. As an iron chelator, DFO can interrupt the Fenton reaction-mediated peroxidation of lipids to inhibit ferroptosis. The treatment efficacy of DOC@TA-Fe^{3+} + DFO was similar to that of DOC via controlling microtubule dynamics. The CT26 tumor-bearing mice were then sacrificed for tumor harvest. As shown in the photographs (Fig. 6B), the volumes of tumors in the DOC@TA-Fe^{3+} group were the smallest because of the combination of microtubule inhibition and ferroptosis therapy. The tumor weights from the mice with different treatments showed the same trend (Fig. S12). Additionally, the body weight of the tumor-bearing mice was monitored during the treatment period (Fig. 6C). No appreciable change in body weight was observed, except in the free DOC group. H&E staining of the major organs was performed, and the results revealed no significant tissue damage (Fig. S13). These results indicated that DOC@TA-Fe^{3+} nanoreactors can improve the safety of DOC in vivo.

Immunohistochemical staining was performed on the tumor tissues. The tumor cells in the control group maintained complete morphology as indicated by H&E staining (Fig. 6D). By contrast, some tumor cells started to lose their cellular integrity after different treatments. Immunohistochemistry analysis was also conducted on Ki67 and CD31 cells (Figs. 6D and S14), and immunofluorescence analysis (Fig. 7) of the terminal deoxynucleotidyl transferase-mediated dUTP nick end labeling and tubulin staining was performed to further elucidate the tumor inhibition mechanism of DOC@TA-Fe^{3+}.

Motivated by the antitumor effect of the DOC@TA-Fe^{3+} nanoreactor observed in the subcutaneous tumor model, we used orthotopic tumor models to further verify the therapeutic efficacy (Fig. 8). We found that compared with those in the control and monotherapy groups, DOC@TA-Fe^{3+} significantly reduced tumor nodules (Figs. 8A and S15), inhibited tumor cell proliferation (Figs. 8B and E) and angiogenesis (Figs. 8C and F), and prolonged mouse survival (Figs. 8D) via the combination of microtubule inhibition and ferroptosis.

4. Conclusion

In this study, we constructed metal-polyphenol supramolecular structures based on TA and iron ions to deliver DOC (DOC@TA-Fe^{3+}) with functions of microtubule inhibition, ROS generation, and GPX4 inhibition for ferroptosis/apoptosis treatment. The DOC@TA-Fe^{3+} nanoreactor can be effectively internalized by tumor cells and can destroy the lysosome membrane through its proton buffer effect, resulting in its escape from the lysosome and the release of antitumor payloads. Because of its strong reducibility, TA can convert Fe^{3+} into Fe^{2+} to efficiently produce a strong Fenton reaction and continuously supply Fe^{3+} for ferroptosis. Additionally, DFO introduction has weakened the antitumor effect of the nanoreactor, further confirming the involvement of the ferroptosis pathway in the antitumor effect. The developed nanoreactor can rapidly accumulate at the tumor site after being injected via the tail vein, suggesting that the nanoreactor can quickly reach the tumor tissue for cancer therapy.

CRediT author statement

Min Mu: Conceptualization, Methodology, Software, Data curation, Writing - Original draft preparation; **Xiaoyan Liang:** Investigation, Data curation, Investigation; **Na Zhao:** Investigation; **Di Chuan:** Validation, Methodology; **Bo Chen:** Methodology; **Shasha Zhao:** Validation; **Guoqing Wang:** Methodology; **Rangrang Fan:** Investigation, Visualization; **Bingwen Zou:** Supervision; **Bo Han:** Supervision; **Gang Guo:** Writing - Reviewing and Editing, Supervision.

Declaration of competing interest

The authors declare that there are no conflicts of interest.

Acknowledgments

Appendix A. Supplementary data

Supplementary data to this article can be found online at https://doi.org/10.1016/j.jpha.2022.09.003.

References

[1] F. Hellal, A. Hurtado, J. Ruschel, et al., Microtubule stabilization reduces scarring and causes axon regeneration after spinal cord injury, Science 331 (2011) 928–931.

[2] M. He, Y. Ding, C. Chu, et al., Autophagy induction stabilizes microtubules and promotes axon regeneration after spinal cord injury, Proc. Natl. Acad. Sci. U S A 113 (2016) 11324–11329.

[3] G. Li, X. Hu, X. Wu, et al., Microtubule-targeted self-assembly triggers prometaphase metaphase oscillations suppressing tumor growth, Nano Lett. 21 (2021) 3052–3059.

[4] C. Dumontet, M.A. Jordan, Microtubule-binding agents: A dynamic field of cancer therapeutics, Nat. Rev. Drug Discov. 9 (2010) 790–803.

[5] J. Kim, J. Lee, J. Lee, et al., Tubulin-based nanotubes as delivery platform for microtubule-targeting agents, Adv. Mater. 32 (2020), e2002902.

[6] T. Feng, J. Wan, P. Li, et al., A novel NIR-controlled NO release of sodium nitroprusside-doped Prussian blue nanoparticle for synergistic tumor treatment, Biomaterials 214 (2019), 119213.

[7] K. Poudel, S. Park, J. Hwang, et al., Photothermally modulatable and structurally disintegratable sub-8-nm Au$_1$Ag$_9$ embedded nanoblocks for combination cancer therapy produced by plug-in assembly, ACS Nano 14 (2020) 11040–11054.

[8] S. Wang, J. Shao, Z. Li, et al., Black phosphorus-based multimodal nanoagent: Showing targeted combinatory therapeutics against cancer metastasis, Nano Lett. 19 (2019) 5587–5594.

[9] J. Tian, B. Huang, H. Li, et al., NIR-activated polymeric nanoplatform with upper critical solution temperature for image-guided synergistic photothermal therapy and chemotherapy, Biomacromolecules 20 (2019) 2338–2349.

[10] S.J. Dixon, K.M. Lemberg, M.R. Lamprecht, et al., Ferroptosis: An iron-dependent form of nonapoptotic cell death, Cell 149 (2012) 1060–1072.

[11] E. Nottingham, E. Mazzio, S.K. Surapaneni, et al., Synergistic effects of methyl 2-cyano-3,11-dioxo-18beta-olean-1,-12-dien-30-oate and erlotinib on erlotinib-resistant non-small cell lung cancer cells, J. Pharm. Anal. 11 (2021) 799–807.

[12] H. Liang, X. Wu, G. Zhao, et al., Renal clearable ultrasmall single-crystal Fe nanoparticles for highly selective and effective ferroptosis therapy and immunotherapy, J. Am. Chem. Soc. 143 (2021) 15812–15823.

[13] S. Xie, W. Sun, C. Zhang, et al., Metabolic control by heat stress determining cell fate to ferroptosis for effective cancer therapy, ACS Nano 15 (2021) 7179–7194.

[14] L.-L. Zhou, Q. Guan, W.-Y. Li, et al., A ferrocene-functionalized covalent organic framework for enhancing chemodynamic therapy via redox dyshomeostasis, Small 17 (2021), e2101368.

[15] L. Zhou, J. Chen, R. Li, et al., Metal-polyphenol-network coated Prussian blue nanoparticles for synergistic ferroptosis and apoptosis via triggered GPX4 inhibition and concurrent *in situ* bleomycin toxification, Small 17 (2021), e2103919.

[16] G. Wang, L. Xie, B. Li, et al., A nanounit strategy reverses immune suppression of exosomal PD-L1 and is associated with enhanced ferroptosis, Nat. Commun. 12 (2021), 5733.

[17] M. Mu, Y. Wang, S. Zhao, et al., Engineering a pH/glutathione-responsive tea polyphenol nanodevice as an apoptosis/ferroptosis-inducing agent, ACS Appl. Bio Mater. 3 (2020) 4128–4138.

[18] S.J. Dixon, B.R. Stockwell, The role of iron and reactive oxygen species in cell death, Nat. Chem. Biol. 10 (2014) 9—17.

[19] T. Ganz, E. Nemeth, Iron homeostasis in host defence and inflammation, Nat. Rev. Immunol. 15 (2015) 500—510.

[20] J.P. Friedmann Angeli, M. Schneider, B. Proneth, et al., Inactivation of the ferroptosis regulator Gpx4 triggers acute renal failure in mice, Nat. Cell Biol. 16 (2014) 1180—1191.

[21] H. He, L. Du, H. Guo, et al., Redox responsive metal organic framework nanoparticles induces ferroptosis for cancer therapy, Small 16 (2020), e2001251.

[22] Y.-J. He, X.-Y. Liu, L. Xing, et al., Fenton reaction-independent ferroptosis therapy via glutathione and iron redox couple sequentially triggered lipid peroxide generator, Biomaterials 241 (2020), 119911.

[23] T. Liu, W. Liu, M. Zhang, et al., Ferrous-supply-regeneration nanoengineering for cancer-cell-specific ferroptosis in combination with imaging-guided photodynamic therapy, ACS Nano 12 (2018) 12181—12192.

[24] E. Sawicki, M.J. Hillebrand, H. Rosing, et al., Validation of a liquid chromatographic method for the pharmaceutical quality control of products containing elacridar, J. Pharm. Anal. 6 (2016) 268—275.

[25] L. Zhang, S.-S. Wan, C.-X. Li, et al., An adenosine triphosphate-responsive autocatalytic Fenton nanoparticle for tumor ablation with self-supplied H_2O_2 and acceleration of Fe(III)/Fe(II) conversion, Nano Lett. 18 (2018) 7609—7618.

[26] C.-C. Xue, M.-H. Li, Y. Zhao, et al., Tumor microenvironment-activatable Fe-doxorubicin preloaded amorphous $CaCO_3$ nanoformulation triggers ferroptosis in target tumor cells, Sci. Adv. 6 (2020), eaax1346.

[27] J. Chen, F. Chen, L. Zhang, et al., Self-assembling porphyrins as a single therapeutic agent for synergistic cancer therapy: A one stone three birds strategy, ACS Appl. Mater. Interfaces 13 (2021) 27856—27867.

[28] C. Pan, M. Ou, Q. Cheng, et al., Z-scheme heterojunction functionalized pyrite nanosheets for modulating tumor microenvironment and strengthening photo/chemodynamic therapeutic effects, Adv. Funct. Mater. 30 (2020), 1906466.

[29] G. Shen, R. Xing, N. Zhang, et al., Interfacial cohesion and assembly of bioadhesive molecules for design of long-term stable hydrophobic nanodrugs toward effective anticancer therapy, ACS Nano 10 (2016) 5720—5729.

[30] Z. Ren, S. Sun, R. Sun, et al., A metal-polyphenol-coordinated nanomedicine for synergistic cascade cancer chemotherapy and chemodynamic therapy, Adv. Mater. 32 (2020), e1906024.

[31] M. Mu, H. Chen, R. Fan, et al., A tumor-specific ferric-coordinated epi-gallocatechin-3-gallate cascade nanoreactor for glioblastoma therapy, J. Adv. Res. 34 (2021) 29—41.

[32] H. Ejima, J.J. Richardson, K. Liang, et al., One-step assembly of coordination complexes for versatile film and particle engineering, Science 341 (2013) 154—157.

[33] Y. Ping, J. Guo, H. Ejima, et al., pH-responsive capsules engineered from metal-phenolic networks for anticancer drug delivery, Small 11 (2015) 2032—2036.

[34] Y. Zheng, X. Li, C. Dong, et al., Ultrasound-augmented nanocatalytic ferroptosis reverses chemotherapeutic resistance and induces synergistic tumor nanotherapy, Adv. Funct. Mater. 32 (2021), 2107529.

[35] M. Mu, X. Liang, D. Chuan, et al., Chitosan coated pH-responsive metal-polyphenol delivery platform for melanoma chemotherapy, Carbohydr. Polym. 264 (2021), 118000.

[36] J. Chen, J. Li, J. Zhou, et al., Metal-phenolic coatings as a platform to trigger endosomal escape of nanoparticles, ACS Nano 13 (2019) 11653—11664.

[37] R. Fan, C. Chen, H. Hou, et al., Tumor acidity and near-infrared light responsive dual drug delivery polydopamine-based nanoparticles for chemo-photo-thermal therapy, Adv. Funct. Mater. 31 (2021), 2009733.

[38] X. Yu, T. Shang, G. Zheng, et al., Metal-polyphenol-coordinated nanomedicines for Fe(II) catalyzed photoacoustic-imaging guided mild hyperthermia-assisted ferroustherapy against breast cancer, Chin. Chem. Lett. 33 (2022) 1895—1900.

[39] Z. Zhang, M. Lu, C. Chen, et al., Holo-lactoferrin: The link between ferroptosis and radiotherapy in triple-negative breast cancer, Theranostics 11 (2021) 3167—3182.

[40] Y. Zhang, K. Xi, X. Fu, et al., Versatile metal-phenolic network nanoparticles for multitargeted combination therapy and magnetic resonance tracing in glioblastoma, Biomaterials 278 (2021) 121163.

[41] S. Wang, F. Li, R. Qiao, et al., Arginine-rich manganese silicate nanobubbles as a ferroptosis-inducing agent for tumor-targeted theranostics, ACS Nano 12 (2018) 12380—12392.

[42] X. Meng, J. Deng, F. Liu, et al., Triggered all-active metal organic framework: Ferroptosis machinery contributes to the apoptotic photodynamic antitumor therapy, Nano Lett. 19 (2019) 7866—7876.

[43] H. Xiong, C. Wang, Z. Wang, et al., Intracellular cascade activated nanosystem for improving ER+ breast cancer therapy through attacking GSH-mediated metabolic vulnerability, J. Control. Release 309 (2019) 145—157.